

Direct Numerical Simulation of Incompressible Flows in a Zero-Pressure Gradient Turbulent Boundary Layer

Chuantan Lin¹ and Zuojin Zhu^{1,*}

¹ *Multiphase Reactive Flow Division, Department of Thermal Science and Energy Engineering, USTC, Hefei, 230026, China*

Received 6 November 2009; Accepted (in revised version) 18 March 2010

Available online 28 May 2010

Abstract. Direct numerical simulation (DNS) of incompressible flows in a zero-pressure gradient turbulent boundary layer (TBL) is conducted by a finite difference method in which a fourth order upwind scheme is applied to discretize the convective terms while a re-scaling approach is used to set inlet flow conditions. The Reynolds numbers based on free flow velocity and momentum thickness at the recycle section are respectively 687, 1074, and 1430. The DNS has obtained favorable results indicating that the turbulence statistics is quite satisfactory as compared with the existing numerical and experimental results. The three dimensional turbulent structures at the momentum thickness Reynolds number of 1430 in several different instants are illustrated by the iso-surface of swirl strength square (the square of imaginary part of the complex eigenvalue of velocity gradient tensor) together with velocity vectors in three different cross sections. It is found that there are three kinds of vortical structures: quasi-symmetrical and asymmetrical hairpin vortices, and worm-like vortices. The DNS based on the numerical method can certainly reveal the main characteristics of the TBL flows at the given Reynolds numbers.

PACS (2006): 47.11.Bc, 47.27.Cn, 47.27.ek, 47.27.nd

Key words: Direct numerical simulation, incompressible boundary layer flows, hairpin vortex, worm-like vortex.

1 Introduction

Zero-pressure gradient turbulent boundary layer (TBL) is a fundamental problem in the study of wall turbulence. Since turbulence plays a very important role in nature, civil and industrial engineering processes, the study of TBL is of great significance in the development of fluid mechanics. To date, much work has been done for the

*Corresponding author.

URL: <http://staff.ustc.edu.cn/~zuojin>

Email: zuojin@ustc.edu.cn (Z. J. Zhu), linchts@mail.ustc.edu.cn (C. T. Lin)

wall turbulence mechanism. The earlier experiments studied the mechanism of turbulence [1], the law of wake in a TBL [2], and the transition from laminar to turbulence [3, 4]. Significantly, a structural model named hairpin vortex was proposed [1] to explain the turbulent production and dissipation in a TBL. Low speed streaks [3] were found in the near wall region by flow visualization.

There were the TBL investigations in the period from 1960 to 1999 in the 20th century. They include the experiments [7–29] and numerical simulations [30–34]. Based on these studies, a consistent view was formed: There are coherent vortex structures in the TBL, leading to the ejection and sweeping of fluid motions that result in the irregular velocity and vorticity fluctuations with broad spatial and temporal scales. The findings of Bandyopadhyay and Head [11, 13] are noteworthy. In the range of momentum thickness Reynolds number from 500 to 1.75×10^4 , hairpin vortex is a crucial feature of a zero-pressure gradient TBL with its shape depending on the Reynolds number. The hairpin vortex has a curve type at low Reynolds numbers, Ω type at moderate Reynolds numbers, and stretched hairpin type at higher Reynolds numbers.

Acarlar and Smith [19, 20] investigated the key role played by hairpin vortices in developing and sustaining the turbulence process in the near-wall region of TBL for the cases of hemisphere pro-turbulence- and fluid ejection-generated hairpin vortices in a developing boundary layer. Using flow visualization and hot film anemometry, they found the primary hairpin vortex can generate a downstream hairpin with a tertiary hairpin vortex occurring between the primary and downstream vortices. The scale of this kind of coherent structure in the main flow direction is several times that of a single hairpin. Strong inflectional profiles were found just downstream of the hairpin-vortex generation region, which evolved into fuller profiles with increasing downstream distance, eventually developing a remarkable similarity to a turbulent boundary layer velocity profile. While high sensitivity to external forcing is noted together with a tendency toward the organized development of larger, and more complex structures through a pairing-type process in the case of fluid ejection generation.

Recent experiments of TBL flows have emphasized the vortex properties [35–37], with DNS works involved with either heat convection [38] or supersonic flow characteristics [39, 40]. To improve the understanding of coherent structures and the scaling of the energy spectra, recent numerical studies have also dedicated turbulent channel flows [41–45]. Adrian [46] and Wallace [47] gave a broad view of the development of near-wall turbulence in their separate review articles.

This paper presents the DNS results of incompressible TBL flows with zero-pressure gradient. A re-scaling approach was used to set inlet flow conditions, and a relatively coarse grid ($241 \times 61 \times 81$) was used in the DNS. The grids in the streamwise and spanwise directions are uniform while in the vertical direction there are 61 grids distributed non-uniformly, with a larger grid density near-wall. The grid resolution is chosen on the basis of the comparison of friction and shape factors with existing results as shown in Fig. 1(a) and (b). In the DNS, the momentum thickness Reynolds numbers at the recycle section are respectively 687, 1074, and 1430. The primary objective of this work is to numerically explore the characteristics of velocity fluctuations and

vortical structures in the TBL. It is revealed that the turbulence statistics is in a good agreement with the existing computational and experimental results. At the Reynolds number of 1430, there are three kinds of vortical structures: quasi-symmetrical and asymmetrical hairpin vortices, and worm-like vortices. The TBL flow contains more asymmetrical hairpin vortices. This is consistent with the previous finding reported by Robinson [32].

2 Governing equations

The governing equations are described in a cartesian coordinate system, where $x(x_1)$, $y(x_2)$ and $z(x_3)$ represent the coordinates in the streamwise, vertical and spanwise directions. The length and velocity scales are assumed to be the momentum thickness at the inlet section $\delta_{2,in}$ and the free flow velocity of boundary layer U_∞ . The time scale is given by $\delta_{2,in}/U_\infty$. The pressure scale is ρU_∞^2 , where ρ is the fluid density. Hence, the normalized governing equations can be written as

$$\nabla \cdot \mathbf{u} = 0, \quad (2.1)$$

$$\mathbf{u}_t + \mathbf{u} \cdot \nabla \mathbf{u} = -\nabla p + \frac{\nabla^2 \mathbf{u}}{\text{Re}}, \quad (2.2)$$

here the Reynolds number Re is defined by the inlet momentum thickness, free flow velocity, and kinematic viscosity of fluid ν , $\text{Re} = U_\infty \delta_{2,in} / \nu$. The initial flow field is assumed to be laminar. The spanwise periodic condition is used with the non-slip conditions on the solid wall. The inlet conditions are set by the re-scaling approach developed by Lund et al. [48]. On the top boundary, we assume

$$\frac{\partial \mathbf{u}}{\partial y} = 0, \quad (2.3)$$

while for the boundary conditions at the outlet, similar to the treatment utilized previously [49,50] we use the Orlanski [51] type

$$\left(\frac{\partial}{\partial t} + U_{\text{out}} \frac{\partial}{\partial x} \right) \mathbf{u} = 0, \quad (2.4)$$

where U_{out} is the outlet-sectionally averaged velocity in the streamwise direction.

3 Numerical method

The normalized size of computational domain is described by $L_x=80$, $L_y=30$, and $L_z=15$. The value of spanwise width L_z is assigned so that at least one low-speed streak can be included in the domain. The non-uniform grids in the y -direction were set according to

$$\frac{y_j}{L_y} = 1 - \frac{\tanh[\alpha(1 - j/N_y)]}{\tanh(\alpha)}, \quad (3.1)$$

where N_y is the total number of vertical grids, and the grid number $j = 0, 1, 2, \dots, N_y$. $\alpha=3.157$, it is used as a parameter to adjust the grid distance to the wall.

The governing equations (2.1) and (2.2) are numerically solved by the accurate projection algorithm PmIII [52] in a non-uniform staggered grid system. Their discretization is accomplished by a finite difference method. Similar to the previous work [53], the non-linear cross-convection terms, such as vu_y , and wu_z in the momentum equation for the velocity in the streamwise direction are treated carefully so that the scheme has a higher accuracy in discretizing the non-linear terms.

As an example, we give the finite difference of term vu_y . In the staggered grid system, since the velocity components $[u_{ijk}, v_{ijk}]$ are respectively located at grid points $(x_{i-1/2}, y_j, z_k)$, and $(x_i, y_{j-1/2}, z_k)$, in the case of $\hat{v}_{ijk}(x_{i-1/2}, y_j, z_k) \geq 0$, the improved higher-order upwind scheme can be written in the following form

$$(vu_y)_{ijk} = \hat{v}_{ijk} \left(- (A + B + C)u_{ijk} + Au_{i,j-1,k} + Bu_{i,j-2,k} + Cu_{i,j+1,k} - D(u_y^{(4)})_{ijk} \right). \tag{3.2}$$

Here $u_y^{(4)}$ denotes the fourth order partial derivative with respect to y . If

$$\delta y_j = y_j - y_{j-1}, \quad s_2 = \frac{\delta y_{j-1} + \delta y_j}{\delta y_j} \quad \text{and} \quad s_3 = \frac{\delta y_{j+1}}{\delta y_j},$$

then the coefficients of the finite difference can be expressed as

$$B = \frac{s_3^3 + s_3^2}{\delta y_j \cdot \Delta}, \quad C = -\frac{s_2^2 - s_2^3}{\delta y_j \cdot \Delta}, \quad A = -Bs_2^2 - Cs_3^2, \tag{3.3}$$

and

$$D = \frac{1}{24} \left\{ A(\delta y_j)^4 + B(\delta y_j + \delta y_{j-1})^4 + C(\delta y_{j+1})^4 \right\}, \tag{3.4}$$

where

$$\Delta = s_2 s_3 (s_2 - 1)(s_3 + 1)(s_2 + s_3).$$

With the application of the Taylor expansion, it is easy to express the cross-convection velocity by an interpolation with operator I_{ijk}^β and a corresponding grid-dependent remainder as follows

$$\hat{v}_{ijk} = I_{ijk}^\beta(v) - R_{ijk} + o(\epsilon^4), \tag{3.5a}$$

$$R_{ijk} = \frac{1}{8} \left\{ (\delta x_i)^2 I_{ijk}^\beta(v_{xx}) + (\delta y_j \delta y_{j+1}) I_{ijk}^\beta \left[v_{yy} + \frac{1}{6} (\delta y_{j+1} - \delta y_j) v_y^{(3)} \right] \right\}, \tag{3.5b}$$

$$I_{ijk}^\beta(v) = \frac{1}{2} \left[\beta(v_{ijk} + v_{i-1,j,k}) + (1 - \beta)(v_{i,j+1,k} + v_{i-1,j+1,k}) \right], \tag{3.5c}$$

where

$$\delta x_i = x_i - x_{i-1}, \quad \beta = \frac{\delta y_{j+1}}{(\delta y_j + \delta y_{j+1})}.$$

$o(\epsilon^4)$ denotes a fourth order cut-off error, R_{ijk} represents the remainder resulted from linear interpolation in terms of operator (I_{ijk}^β). The difference from the previous scheme given in [54] lies in the deduction of this interpolation remainder, which obviously enhances the accuracy of finite difference for the cross-convection term vu_y . Clearly, similar expressions can be derived for the finite difference of other cross convection terms, i.e., wu_z in the streamwise momentum equation, $[uv_x, wv_z]$ in the vertical momentum equation and $[uw_x, vw_y]$ in spanwise momentum equation.

Let the intermediate velocity vector, the pressure potential and the time level be denoted by $\bar{\mathbf{u}}$, ϕ and n , respectively. Assuming

$$\mathbf{H} = (\mathbf{u} \cdot \nabla) \mathbf{u},$$

we have

$$\mathbf{u}^{n+1} = \bar{\mathbf{u}} - \Delta t \nabla \phi, \quad (3.6)$$

$\bar{\mathbf{u}}$ can be calculated by

$$\frac{\bar{\mathbf{u}} - \mathbf{u}^n}{\Delta t} + \mathbf{H}^{n+\frac{1}{2}} = \frac{1}{\text{Re}} \nabla^2 \left[\mathbf{u}^n + \frac{1}{2} (\bar{\mathbf{u}} - \mathbf{u}^n) \right], \quad (3.7)$$

and pressure p by

$$p^{n+\frac{1}{2}} = \left(1 - \frac{\Delta t}{2\text{Re}} \nabla^2 \right) \phi, \quad (3.8)$$

where the pressure potential ϕ must satisfy the Poisson's equation

$$\nabla^2 \phi = \nabla \cdot \frac{\bar{\mathbf{u}}}{\Delta t}. \quad (3.9)$$

In addition, for the calculation of intermediate velocity $\bar{\mathbf{u}}$, the convection terms were treated explicitly by the second order Adams-Bashforth scheme, and calculated by a blocked tri-diagonal matrix acceleration (TDMA) in the spanwise direction due to the periodic boundary condition. The pressure potential Poisson's equation was at first solved by the approximate factorization one (AF1) method [55], and a pressure potential field with improved accuracy was then obtained using the stabilized bi-conjugate gradient method (Bi-CGSTAB) proposed by Van der Vorst [56].

4 Results and discussion

The incompressible TBL flows at three Reynolds numbers based on the momentum thickness (687, 1074, and 1430) were numerically studied. The calculation was carried out in a staggered grid system, with the non-uniform grids in the normal direction generated by a tangent function. The parameters of calculation are given in Table 1.

Table 1: The parameters of calculation.

Re*	Re ₂	$\Delta L_{in,re}^+$ [†]	Δx^+	Δy_{min}^+	Δy_{max}^+	Δz^+
625	687	1519	10.1	0.37	48.1	5.7
1000	1074	2285	15.2	0.55	72.2	8.6
1320	1430	2864	19.1	0.69	90.7	10.7

*Defined by free velocity and momentum thickness at the inlet section.

[†]Here the superscript shows that the length is normalized by ν/u_τ at the recycle section.

The inlet Reynolds number and the Reynolds number at the re-cycled section are defined by Re and Re₂, respectively, while the distance from the recycled section to the inlet section is defined by $\Delta L_{in,re}^+$. The turbulence states at the recycled section were extracted for the statistical analysis, in which the mean values were taken by an average in the z -direction and time. The data were saved in a time interval of 0.4 in the totally sampling time period of 1000. The numerical work focuses on

1. Exploring turbulence characteristics by statistical analysis, and determining the Reynolds number effect on the numerical results;
2. Finding instantaneous turbulent flow structures by observing the iso-surface of swirl strength square and the velocity vectors in the TBL.

4.1 Turbulence statistics

Based on the average in the spanwise direction and time, statistical values of turbulent variables at the recycle section were evaluated. The recycle section was chosen downstream of the inlet section with a distance large enough as compared to the maximum streamwise scale of velocity streaks, which is usually over 1000 wall unit (ν/u_τ). The distance values were listed in the third column of Table 1. The initial field was obtained by perturbing a smooth laminar boundary layer. The statistical analysis of the simulation data has indicated the friction and shape factors, the turbulence intensities in the near wall region ($y^+ \leq 60$), the mean velocity profile and Reynolds shear stress in the TBL.

The friction factor defined by

$$C_f = \frac{2\tau_w}{\rho U_\infty^2} = \frac{2\nu(\partial u/\partial y)_w}{U_\infty^2},$$

and the shape factor defined by the ratio of displacement thickness (δ_1) to the momentum thickness (δ_2), $H = \delta_1/\delta_2$, are plotted as functions of the momentum thickness Reynolds number Re₂ (based on the thickness δ_2), as shown in Fig. 1 (a) and (b). The presently obtained values are shown by filled circles, together with the existing results of Coles [2], Spalart [31], and other researchers [15, 16]. The results of current calculation agree well with the published data. As compared to the calculation of Spalart [31],

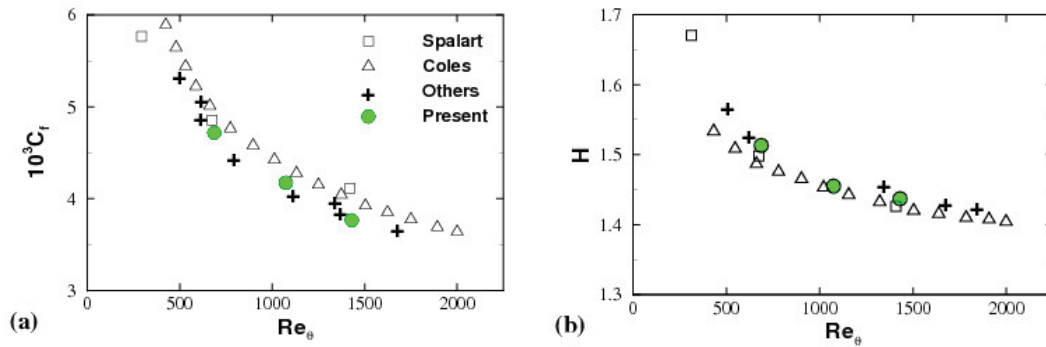


Figure 1: The friction factor (a) and shape factor (b) plotted as functions of the momentum thickness Reynolds number.

the C_f values are slightly smaller, and the H values are slightly large, indicating that the ratio of friction velocity to free velocity at the recycle section in the present calculation is relatively low. The reason causing these slight differences can be traced in numerical aspect. Spalart [31] obtained his results using a spectral method with up to about 10^7 grid points, in which a multiple-scale procedure is applied to approximate the slow streamwise growth of the boundary layer.

The mean velocity profile in the TBL is shown in Fig. 2. A comparison of the calculated velocity profile with the existing profiles indicates that they are a good agreement. It is seen that the profile collapses the numerical result of Spalart [31] and the experimental result of Adrian [35]. The calculated results are also consistent with the DNS result of Kim et al. [41] for turbulent channel flow, and the profile along the wall bisector of a square duct given by Yang et al. [53]. In the sublayer of $y^+ \leq 5$, the calculated profile fits in with the law of wall given by $U^+ = y^+$; while in the logarithmic region of $y^+ \geq 30$, it fits in with the log law given by $U^+ = 2.44 \ln(y^+) + 5.2$. In the outer region of the TBL, $y > 0.2\delta_1$, the velocity profile satisfies a defective law, $(U - U_\infty)/u_\tau = f(\eta)$, here $\eta = y/\delta_1$.

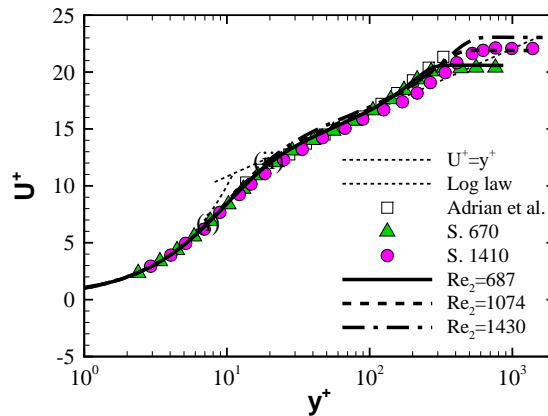


Figure 2: The mean velocity profile in the turbulent boundary layer. Note that the log-law is given by $U^+ = 2.44 \ln(y^+) + 5.2$.

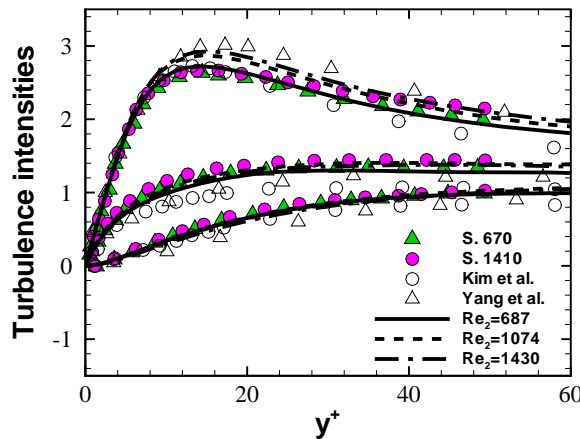


Figure 3: The turbulent intensities in the inner layer of turbulent boundary layer.

The turbulence intensities in the near wall region of the TBL ($y^+ \leq 60$) are plotted as functions of wall coordinate y^+ , as shown in Fig. 3. It is seen that the turbulence intensity curves accord well with the results reported by Spalart [31] for TBL calculation, by Kim et al. [41] for turbulent channel flow, and by Yang et al. [53] for turbulent square duct flow. For TBL flow at the three Reynolds numbers, $Re_2=687, 1074,$ and $1430,$ the peak value of u_{rms} occurs in the buffer given by $5 < y^+ < 30,$ it is larger than w_{rms} with a factor of about $2 \sim 3;$ relative to $v_{rms},$ the factor is about $3 \sim 6.$ This suggests that the velocity fluctuation in buffer should be highly anisotropic due to the interaction of vortices and the solid wall. The wall effect makes the constrained fluid motion in the normal to wall direction, leading to a smaller velocity fluctuation. Beyond the buffer, with the increase of the distance to wall, the wall effect becomes weaker and the flow anisotropy decreases.

A comparison of turbulent Reynolds shear stress in the TBL is shown in Fig. 4, where the measured results of Adrian et al. [35] and Balint et al. [23] are labeled by

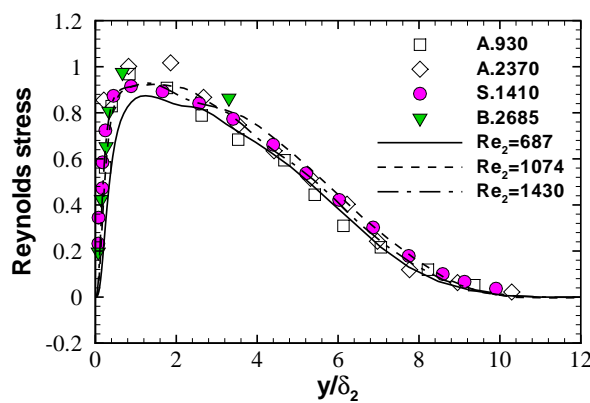


Figure 4: The Reynolds stress $-\langle u'v' \rangle / u_\tau^2$ plotted as a function of $y/\delta_2.$

A.930, A.2370 and B.2685, respectively. The calculation results of Spalart [31] are labeled by S.670 and S.1410. The capital in labeling string represents the first letter of the researcher name, with the followed number denoting the value of Reynolds number based on momentum thickness. From Fig. 4, it is seen that the present calculation generates satisfactory Reynolds stress, which is close to zero at the wall and the outer marginal region of the TBL, and arrives at its peak value close to unity in the unit of $(-u_{\tau}^2)$. The peak occurs at a normal distance to wall of about δ_2 .

4.2 Reynolds number effects

The Reynolds number effect can be clearly seen in Fig. 1. The friction and shape factors decrease monotonically with the Reynolds number Re_2 based on momentum thickness. Previous studies [29,31] have also shown that the turbulent intensity in streamwise direction has a distinct values at $y^+ \approx 15$, and that the y^+ locations of the peaks of the turbulent intensities in other directions and the Reynolds shear stress $-\langle u'v' \rangle^+$ increase with Re_2 . As reported by Antonia and Kim [42], the low-Reynolds-number effect could be explained by an intensification of the vortices in the wall region, even though the average, location and diameter of the vortices were approximately unchanged when expressed in the wall units. The present calculation reveals that the near wall vortex motion is closely related to the coherent motion of hairpin vortices, which travel downward together with worm-like vortices. For the TBL at $Re_2=1430$, the vortices at several different instants will be shown in the next subsection by the iso-surface of swirl intensity square at a value of 4, together with the nearby flow fields illustrated by velocity vectors.

4.3 Vortices

The DNS has revealed that the typical vortices in a TBL at $Re_2=1430$ are quasi symmetrical and asymmetrical hairpin vortices, and worm-like vortices, as illustrated in Figs. 5-9. The hairpins form in the near wall layer, and develop in the log region. The scale of hairpin in the near wall layer is smaller.

Based on previously published experiments [35,37], it is clear to date that the number of hairpins in a packet increases with the increase of Reynolds number. The signature pattern of hairpin consists of a spanwise vortex core located above a region of strong ejection events that occur on a locus inclined at $30-60^\circ$ to the wall. The traveling and coherent motions of these hairpin vortices have substantial impacts on the turbulence fluctuations in the log region and beyond. A review on hairpin vortex organization in wall turbulence is reported recently by Adrian [46].

Because of vortex interaction by mutual stretching, there are a fat lot of fully symmetrical hairpin vortices. The two shoulders usually distribute quasi symmetrically or asymmetrically to the head of a hairpin. A quasi-symmetrical hairpin vortex is illustrated by the iso-surface of the swirl strength square labeled by 4, as seen in Fig. 5(a). This hairpin is of traditional type, which has head, shoulders, and legs. It is consistent

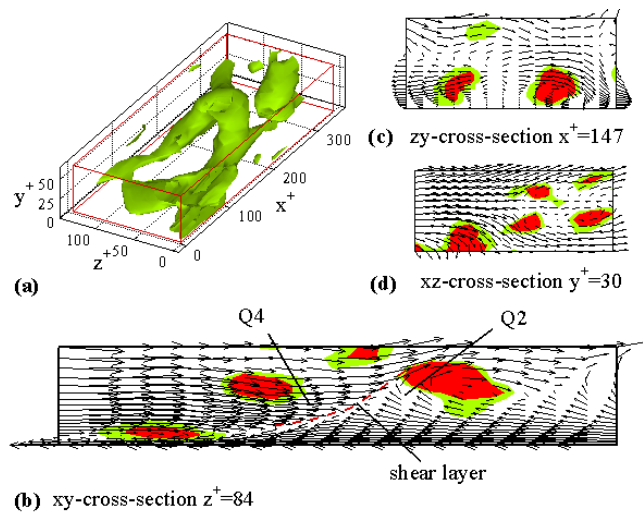


Figure 5: (a) Traditional hairpin vortex; and velocity vector diagrams in (b) xy -cross-section $z^+ = 84$; (c) zy -cross-section $x^+ = 147$; (d) xz -cross-section $y^+ = 30$. Note that the flood-type contours of λ_{ci}^2 are also shown in parts (b-d), where the contours are labeled by 0, 4, and 8.

with the vortical structure proposed by Theodorsen [1]. Its head is in the log region, with legs in the buffer. In Fig. 5(b), the contours of the swirl strength square are shown in a flood form, together with the velocity vectors in the xy -cross section of $z^+ = 84$. A shear layer occurs upstream the hairpin head, under which the ejection or Q2 events are observable due to the vortex rolling up effect while sweep or Q4 events appear upstream of the shear layer. Estimated from the shear layer shape layer shown by dashed line in Fig. 5(b), the inclination of near wall hairpin legs is about 12° . The hairpin vortex shown in Fig. 5(a) is in its early developing stage, since compared with developed

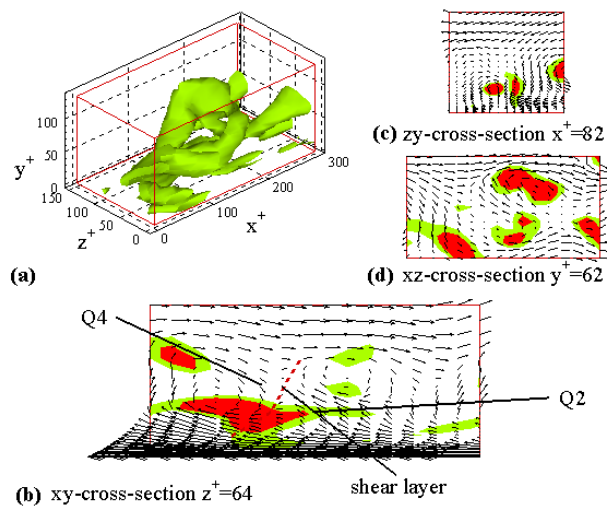


Figure 6: (a) Leg-crossed vortex; and velocity vector diagrams in (b) xy -cross-section $z^+ = 64$; (c) zy -cross-section $x^+ = 82$; (d) xz -cross-section $y^+ = 60$. The flood-type contours of λ_{ci}^2 in parts (b-d) are labeled by the same values as in Fig. 5, and are those given in Figs. 7-9.

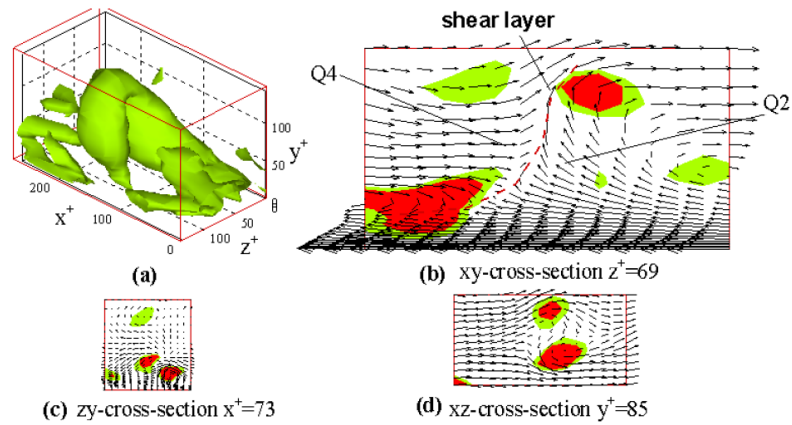


Figure 7: (a) Asymmetrical hairpin vortex; and velocity vector diagrams in (b) xy -cross-section $z^+ = 69$; (c) zy -cross-section $x^+ = 73$; (d) xz -cross-section $y^+ = 85$.

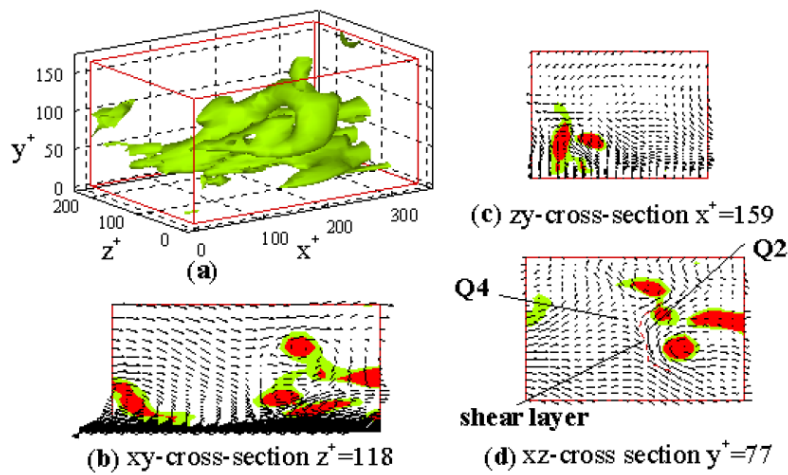


Figure 8: (a) Distorted hairpin vortex; and velocity vector diagrams in (b) xy -cross-section $z^+ = 118$; (c) zy -cross-section $x^+ = 159$; (d) xz -cross-section $y^+ = 77$.

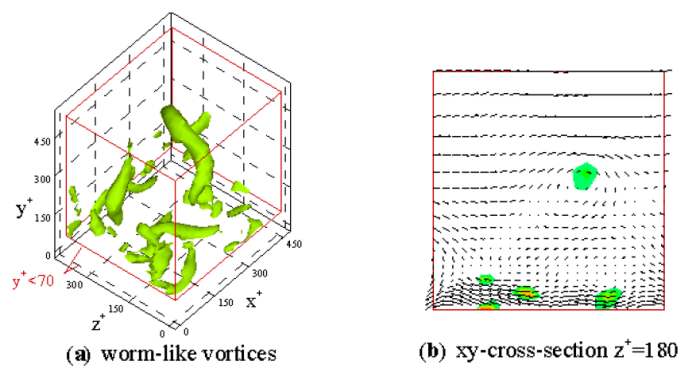


Figure 9: (a) Worm-like vortices; and velocity vector diagrams in (b) xy -cross-section $z^+ = 180$.

Ω type hairpins [Fig. 6(a)], the length and width scales are smaller, respectively, 150 and 100 in the wall unit (ν/u_τ).

The flow patterns around the hairpin can be seen in the slices of $x^+=147$, and $y^+=30$, as shown in Fig. 5 (b) and (c). The flow pattern in the slice of $x^+=147$ is similar to a mushroom, implying that the left leg of the hairpin occurring at a comparatively large z^+ value contains anticlockwise rotating secondary vortices, while the right leg contains clockwise rotating secondary vortices. In Fig. 5(d), in addition to the vortex near the frontal side of $z^+=0$, there is a counter rotating vortex pair upstream of the vortex pair corresponding to the hairpin shoulders. This indicates that the hairpin legs have connected up two vortex tubes with negative inclination angles to the wall. The upstream vortex pair transports fluids between the two vortices to outer sides, while the vortex pair relevant to the hairpin shoulders plays the reverse role, transporting outer side fluids to the inside region.

Another quasi-symmetrical hairpin can be found in Fig. 6(a). This hairpin results from the further development of near wall hairpins, occurs in the log region of TBL, and has a longer length scale in comparison with the hairpin shown in Fig. 5(a). The leg-crossed hairpin head inclines to the wall at an angle of about 60° ; the Q4 and Q2 events are active in a larger nearby region, as seen in Fig. 6(b). The cause of leg-crossing can be traced to the evolution of hairpin under the conditions of vortical interaction, stretching and distorting. The hairpin leg-crossing leads to the secondary flow in the slice of $x^+=82$ has a core-closed vortex pair [Fig. 6(c)]. The right shoulder of the hairpin tends towards break, since the flow pattern in the slice of $y^+=62$ shows that the relevant vertical vortex has double-core [Fig. 6(d)].

As shown in Fig. 7(a), the hairpin is evidently asymmetrical, its head occurs in the log region of the TBL, its right leg is longer and crassitude, its left leg is exiguous and short. The flow patterns around the asymmetrical hairpin can be seen in Fig. 7 (b) and (d).

Another asymmetrical hairpin can be seen in Fig. 8(a). This hairpin is apparently rotated, almost facing to the z direction. Therefore, the Q2, Q4, and shear layer should be labeled in a slice of constant y^+ , as shown in Fig. 8(d). The flow patterns in the slices of $z^+=118$ and $x^+=159$ illustrated in Fig. 8(b) and (c) indicates the hairpin is really asymmetrical in shape.

As shown in Fig. 9(a) and (b), in the outer region of TBL, there are worm-like vortices that are likely generated by the break of hairpins. They look like vortex tubes with the spatial scale varying with the distance from the solid wall. The inner side worms are in general smaller in size.

5 Conclusions

Incompressible flows in a zero-pressure gradient TBL have been studied by DNS with a finite difference method using a comparatively coarse grid. Turbulence statistics has been analysed with the data acquired in recycle section. It was shown that the veloc-

ity profile, turbulence intensities and turbulent shear stress are in a good agreement with the existing numerical and experimental results. Worm-like vortices are found in the outer region, but their sizes are smaller in the inner side. Quasi-symmetrical and asymmetrical hairpins are found in buffer and log region of the TBL. Because of the vortex interaction, stretching and distortion, the hairpins appear in deformed shapes, suggesting that the turbulence structures in the TBL are certainly rather complicated.

Acknowledgments

This work was supported by NSFC (90815030).

References

- [1] T. THEODORSEN, *Mechanism of turbulence*, Proc. Second Midwestern Conference on Fluid Mechanics, Ohio State University, Columbus, Ohio, 1952, pp. 17–19.
- [2] D. E. COLES, *The law of the wake in the turbulent boundary layer*, J. Fluid. Mech., 1 (1956), pp. 191–226.
- [3] F. R. HAMA, J. D. LONG, J. C. HEGARTY, *On transition to laminar to turbulent flow*, J. Appl. Phys., 28 (1957), pp. 388–394.
- [4] J. H. PRESTON, *The minimum Reynolds number for a turbulent boundary layer and the selection of a transition device*, J. Fluid. Mech., 3 (1957), pp. 373–384.
- [5] S. J. KLINE, W. C. REYNOLDS, F. A. SCHRAUB, P. W. RUNSTADLER, *The structure of turbulent boundary layer*, J. Fluid. Mech., 30 (1967), pp. 741–773.
- [6] D. J. TOWNSEND, *Some new correlation measurements in a turbulent boundary layer*, J. Fluid. Mech., 28 (1967), pp. 439–462.
- [7] E. R. CORINO, R. S. BRODDKEY, *A visual investigation of wall region in turbulent flow*, J. Fluid. Mech., 37 (1969), pp. 1–30.
- [8] L. S. G. KOVASZNAY, V. KIBENS, R. F. BLACKWELDER, *Large-scale motion in the intermittent region of a turbulent boundary layer*, J. Fluid. Mech., 41 (1970), pp. 283–326.
- [9] H. T. KIM, S. J. KLINE, W. C. REYNOLDS, *The production of turbulence near a smooth wall in a turbulent boundary layer*, J. Fluid. Mech., 50 (1971), pp. 133–160.
- [10] G. R. OFFEN, S. J. KLINE, *A proposed model of the bursting process in turbulent boundary layer*, J. Fluid. Mech., 70 (2) (1975), pp. 209–228.
- [11] P. BANDYOPADHYAY, *Large structure with a characteristic upstream interface in turbulent boundary layers*, Phys. Fluids., 23 (1980), pp. 2326–2327.
- [12] C. S. SUBRAMANIAN, R. A. ANTONIA, *Effect of Reynolds number on slightly heated turbulent boundary layer*, Int. J. Heat. Mass. Trans., 24 (1981), pp. 1833–1846.
- [13] M. R. HEAD, P. BANDYOPADHYAY, *New aspects of turbulent boundary layer structures*, J. Fluid. Mech., 107 (1981), pp. 297–337.
- [14] B. J. CANTWELL, *Organized motions in turbulent flow*, Ann. Rev. Fluid. Mech., 13 (1981), pp. 457–515.
- [15] L. P. PURTELL, P. S. KLEBANOFF, F. T. BUCKLEY, *Turbulent boundary layer at low Reynolds numbers*, Phys. Fluids., 24 (1981), pp. 802–811.
- [16] R. D. MURLIS, H. M. TSAI, P. BRADSHAW, *The structure of turbulent boundary layers at low Reynolds numbers*, J. Fluid. Mech., 122 (1982), pp. 13–56.

- [17] C. R. SMITH, S. P. METZLER, *The characteristics of low-speed streaks in the near-wall region of a turbulent boundary layer*, J. Fluid. Mech., 129 (1983), pp. 27–54.
- [18] D. G. BAGARD, W. G. TIEDERMAN, *Burst detection with single-point velocity measurements*, J. Fluid. Mech., 162 (1986), pp. 389–413.
- [19] M. S. ACARLAR, C. R. SMITH, *A study of hairpin vortices in a laminar boundary layer. Part 1: hairpin vortices generated by a hemisphere pro-turbulence*, J. Fluid. Mech., 175 (1987), pp. 1–41.
- [20] M. S. ACARLAR, C. R. SMITH, *A study of hairpin vortices in a laminar boundary layer. Part 2: hairpin vortices generated by fluid injection*, J. Fluid. Mech., 175 (1987), pp. 42–83.
- [21] S. L. LYNOS, T. J. HANRATTY, J. B. MCLAUGHLIN, *Turbulence-producing eddies in the viscous wall region*, AIChE. J., 35 (12) (1989), pp. 1962–1974.
- [22] M. S. CHONG, A. E. PERRY, B. J. CANTWELL, *A general classification of three-dimensional flow fields*, Phys. Fluids., 2 (1990), pp. 765–777.
- [23] P. VUKOSLAVCEVIC, J. M. WALLACE, J. L. BALINT, *The velocity and vorticity vector fields of a turbulent boundary layer, I: simultaneous measurement by hot-wire anemometry*, J. Fluid. Mech., 288 (1991), pp. 21–51.
- [24] J. L. BALINT, J. M. WALLACE, P. VUKOSLAVCEVIC, *The velocity and vorticity vector fields of a turbulent boundary layer, II: statistical properties*, J. Fluid. Mech., 288 (1991), pp. 53–86.
- [25] C. R. SMITH, J. D. WALKER, A. H. HAIDARI, U. SOBRUN, *On the dynamics of near-wall turbulence*, Phil. Trans. Roy. Soc. Lond. A., 336 (1991), pp. 131–175.
- [26] A. H. HAIDARI, C. R. SMITH, *The generation and regeneration of single hairpin vortices*, J. Fluid. Mech., 277 (1994), pp. 135–162.
- [27] S. TARDU, *Characteristics of single and cluster of bursting events in the inner layer. I: vita events*, Exp. Fluids., 20 (1995), pp. 112–124.
- [28] C. D. MEINHART, R. J. ADRIAN, *On the existence of uniform momentum zones in a turbulent boundary layer*, Phys. Fluids., 7 (4) (1995), pp. 694–696.
- [29] C. Y. CHING, L. DJENIDI, R. J. ANTONIA, *Low-Reynolds-number effects in a turbulent boundary layer*, Exp. Fluids., 19 (1995), pp. 61–68.
- [30] P. R. SPALART, A. LEONARD, *Direct numerical simulation of equilibrium turbulent boundary layers*, Proc. 5th Symp. on Turbulent Shear Flows, Ithaca, NY, 1985, 9.35–9.40.
- [31] P. R. SPALART, *Direct numerical simulation of turbulent boundary layer up to $Re=1410$* , J. Fluid Mech., 187 (1988), pp. 61–98.
- [32] S. K. ROBINSON, *Coherent motions in turbulent boundary layer*, Annu. Rev. Fluid. Mech., 23 (1991), pp. 601–639.
- [33] S. LEE, S. K. LELE, P. MOIN, *Simulation of spatially evolving turbulence and applicability of Taylor's hypothesis in compressible flow*, Phys. Fluids., 4 (1992), pp. 1521–1545.
- [34] M. RAIN, P. MOIN, *Direct numerical simulation of spatially evolving turbulence and boundary layer*, J. Comput. Phys., 109 (1993), pp. 169–184.
- [35] R. J. ADRIAN, C. D. MEINHART, C. D. TOMKINS, *Vortex organization in the outer region of turbulent boundary layer*, J. Fluid. Mech., 422 (2000), pp. 1–53.
- [36] C. D. TOMKINS, R. J. ADRIAN, *Spanwise structure and scale growth in turbulent boundary layers*, J. Fluid. Mech., 162 (2003), pp. 389–413.
- [37] B. GANAPATHISUBRAMANI, E. K. LONGMIRE, I. MARUSIC, *Experimental investigation of vortex properties in a turbulent boundary layer*, Phys. Fluids., 18 (2006), 155105.
- [38] H. KONG, H. CHOI, J. S. LEE, *Direct numerical simulation of turbulent thermal boundary layers*, Phys. Fluids., 12 (2000), pp. 2555–2568.
- [39] S. E. GUARINI, R. D. MOSER, K. SHARIFF, A. WRAY, *Direct numerical simulation of supersonic turbulent boundary layer at March 2.5*, J. Fluid. Mech., 414 (2000), pp. 1–33.

- [40] T. MAEDER, N. A. ADAMS, L. KLEISER, *Direct numerical simulation of turbulent supersonic boundary layers by an extended temporal approach*, J. Fluid. Mech., 429 (2001), pp. 187–216.
- [41] J. KIM, P. MOIN, R. MOSER, *Turbulence statistics in fully developed channel flow at low Reynolds number*, J. Fluid. Mech., 177 (1987), 133–166.
- [42] R. A. ANTONIA, J. KIM, *Low-Reynolds-number effects on near wall turbulence*, J. Fluid. Mech., 276 (1994), pp. 61–80.
- [43] D. K. HEIST, T. J. HANRATTY, Y. NA, *Observation of the formation of streamwise vortices by rotation of arch vortices*, Phys. Fluids., 12 (2000), pp. 2965–2975.
- [44] W. SCHOPPA, F. HUSSAIN, *Coherent structures generation in near-wall turbulence*, J. Fluid. Mech., 453 (2002), pp. 57–108.
- [45] J. C. DEL ÁLAMO, J. JIMÉNEZ, P. ZANDONADE, R. D. MOSER, *Scaling of the energy spectra of turbulent channels*, J. Fluid. Mech., 500 (2004), pp. 135–144.
- [46] R. J. ADRIAN, *Hairpin vortex organization in wall turbulence*[J], Phys. Fluids., 19 (2007), 041301.
- [47] J. M. WALLACE, *Twenty years of experimental and direct numerical simulation access to the velocity gradient tensor: what have we learned about turbulence*, Phys. Fluids., 21 (2009), 021301.
- [48] T. S. LUND, X. WU, K. S. SQUIRES, *Generation of turbulent inflow data for spatially-developing boundary layer simulation*, J. Comput. Phys., 140 (1998), pp. 233–257.
- [49] A. SOHANKAR, C. NORBERG, L. DAVIDSON, *Simulation of three-dimensional flow around a square cylinder at moderate Reynolds numbers*, Phys. Fluids., 11 (1999), pp. 288–306.
- [50] A. K. SAHA, G. BISWAS, K. MURALIDHAR, *Three-dimensional study of flow past a square cylinder at low Reynolds numbers*, Int. J. Heat. Fluid. Flow., 24 (2003), pp. 54–66.
- [51] I. ORLANSKI, *A simple boundary condition for unbounded flows*, J. Comput. Phys., 21 (1976), pp. 251–269.
- [52] D. L. BROWN, R. CORTEZ, M. L. MINION, *Accurate projection methods for the incompressible Navier-Stokes equations*, J. Comput. Phys., 168 (2001), pp. 464–499.
- [53] H. X. YANG, T. Y. CHEN, Z. J. ZHU, *Numerical study of forced turbulent heat convection in a straight square duct*, Int. J. Heat. Mass. Trans., 52 (2009), pp. 3128–3136.
- [54] J. L. NIU, Z. J. ZHU, *Numerical simulation of three-dimensional flows around two identical square cylinders in staggered arrangements*, Phys. Fluids., 18 (2006), 044106.
- [55] T. J. BAKER, *Potential flow calculation by the approximate factorization method*, J. Comput. Phys., 42 (1981), pp. 1–19.
- [56] H. A. VAN DER VORST, *BiCGSTAB: A fast and smoothly converging variant of BICG for the solution of non-symmetric linear system*, SIAM. J. Sci. Stat. Comp., 13 (1992), pp. 631–644.